



Interplanetary Shocks between 0.3 and 1.0 au: Helios 1 and 2 Observations

Rajkumar Hajra¹ , Bruce T. Tsurutani² , Gurbax S. Lakhina³, Quanming Lu^{1,4} , Aimin Du^{5,6}, and Lican Shan^{6,7} ¹ CAS Key Laboratory of Geospace Environment, School of Earth and Space Sciences, University of Science and Technology of China, Hefei, People's Republic of China; rajkumarhajra@yahoo.co.in, rhajra@ustc.edu.cn² Retired, Pasadena, California, USA³ Indian Institute of Geomagnetism, Navi Mumbai, India⁴ CAS Center for Excellence in Comparative Planetology, Hefei, People's Republic of China⁵ CAS Engineering Laboratory for Deep Resources Equipment and Technology, Institute of Geology and Geophysics, Chinese Academy of Sciences, Beijing, People's Republic of China⁶ College of Earth and Planetary Sciences, Chinese Academy of Sciences, Beijing, People's Republic of China⁷ Innovation Academy for Earth Science, Chinese Academy of Sciences, Beijing, People's Republic of China

Received 2023 March 28; revised 2023 April 26; accepted 2023 May 7; published 2023 July 4

Abstract

The Helios 1 (H1) and Helios 2 (H2) spacecraft measured the solar winds at a distance between ~ 0.3 and 1.0 au from the Sun. With increasing heliocentric distance (r_h), the plasma speed is found to increase at $\sim 34\text{--}40 \text{ km s}^{-1} \text{ au}^{-1}$ and the density exhibits a sharper fall (r_h^{-2}) compared to the magnetic field magnitude ($r_h^{-1.5}$) and the temperature ($r_h^{-0.8}$). Using all available solar wind plasma and magnetic field measurements, we identified 68 and 39 fast interplanetary shocks encountered by H1 and H2, respectively. The overwhelming majority (85%) of the shocks are found to be driven by interplanetary coronal mass ejections (ICMEs). While the two spacecraft encountered more than 73 solar wind high-speed streams (HSSs), only $\sim 22\%$ had shocks at the boundaries of corotating interaction regions (CIRs) formed by the HSSs. All of the ICME shocks were found to be fast forward (FF) shocks; only four of the CIR shocks were fast reverse shocks. Among all ICME FF shocks (CIR FF shocks), 60% (75%) are quasi-perpendicular with shock normal angles ($\theta_{Bn} \geq 45^\circ$) relative to the upstream ambient magnetic field, and 40% (25%) are quasi-parallel ($\theta_{Bn} < 45^\circ$). No radial dependences were found in FF shock normal angle and speed. The FF shock Mach number (M_{ms}), magnetic field, and plasma compression ratios are found to increase with increasing r_h at the rates of 0.72, 0.89, and 0.98 au^{-1} , respectively. On average, ICME FF shocks are found to be considerably faster ($\sim 20\%$) and stronger (with $\sim 28\%$ higher M_{ms}) than CIR FF shocks.

Unified Astronomy Thesaurus concepts: [Interplanetary shocks \(829\)](#); [Solar coronal mass ejections \(310\)](#); [Corotating streams \(314\)](#); [Interplanetary discontinuities \(820\)](#); [Interplanetary medium \(825\)](#)

1. Introduction

Fast mode (magnetosonic) shocks in the interplanetary medium result from the interaction between transient solar phenomena, such as coronal mass ejections (CMEs) and solar wind high-speed streams (HSSs), and the quiet upstream solar winds (Gold 1955; Sagdeev 1966; Hudson 1970; Tsurutani et al. 2011). The specific properties of interplanetary shocks, such as the magnetosonic Mach number and the shock normal angle, are important features in space plasma physics because they are associated with the heating and compression of the upstream plasma and magnetic fields, thus altering the local solar wind (Kennel et al. 1985; Papadopoulos 1985). CME shocks accelerate solar energetic particles (SEPs) from their formation close to the Sun (Tsurutani et al. 2003) to 1 au and beyond (Tsurutani et al. 1982; Tsurutani & Lin 1985; Reames 1999; Kallenrode 2003; Zank et al. 2006; Reames 2013). The efficiency of the SEP acceleration depends on the shock Mach number and the shock normal angles (Pesses et al. 1979; Tsurutani et al. 1982; Tsurutani & Lin 1985; Reames 1999; Desai & Giacalone 2016; Anastasiadis et al. 2019, and references therein).

The shock Mach number depends on the speed of the interplanetary CME (ICME) relative to the upstream

interplanetary medium, the upstream slow solar wind speed, and the upstream magnetosonic wave speed (Tsurutani et al. 2011, 2021). All three parameters vary as a function of radial distance from the Sun. In particular, ICMEs are known to be accelerated close to the Sun and then possibly decelerated further from the Sun as the shocks pile up more mass in the sheath ahead of the ICME (mass loading of the ICME: Chen & Krall 2003; Zhang et al. 2004; Temmer et al. 2010; Zhuang et al. 2022). These velocity variations will affect the shock Mach number, and thus the Mach number may vary as a function of radial distance.

The shock normal angle depends on the upstream interplanetary magnetic field (IMF) direction. The Parker magnetic field direction (Parker 1958) is radial near the Sun and is more likely $\sim 45^\circ$ near 1.0 au. Thus, one might expect a preponderance of quasi-parallel shocks near the Sun and more quasi-perpendicular shocks near 1.0 au. However, the IMF has large angular variability (Thomas & Smith 1981; Tsurutani et al. 1990). It is sometimes in an “ortho-spiral direction,” perpendicular to the nominal Parker direction. There are also many discontinuities in space that can affect the local shock normal angles (Tsurutani & Smith 1979; Lepping & Behannon 1986; Tsurutani & Ho 1999; Tsurutani et al. 2011). Shocks may also have “waves” on their surface and may disappear and reform (Dryer 1975; Gloeckler et al. 1994, 2001; Pitřna et al. 2021, and references therein).

HSSs emanating from solar coronal holes can interact with the upstream ambient slow solar wind forming corotating



Original content from this work may be used under the terms of the [Creative Commons Attribution 4.0 licence](#). Any further distribution of this work must maintain attribution to the author(s) and the title of the work, journal citation and DOI.

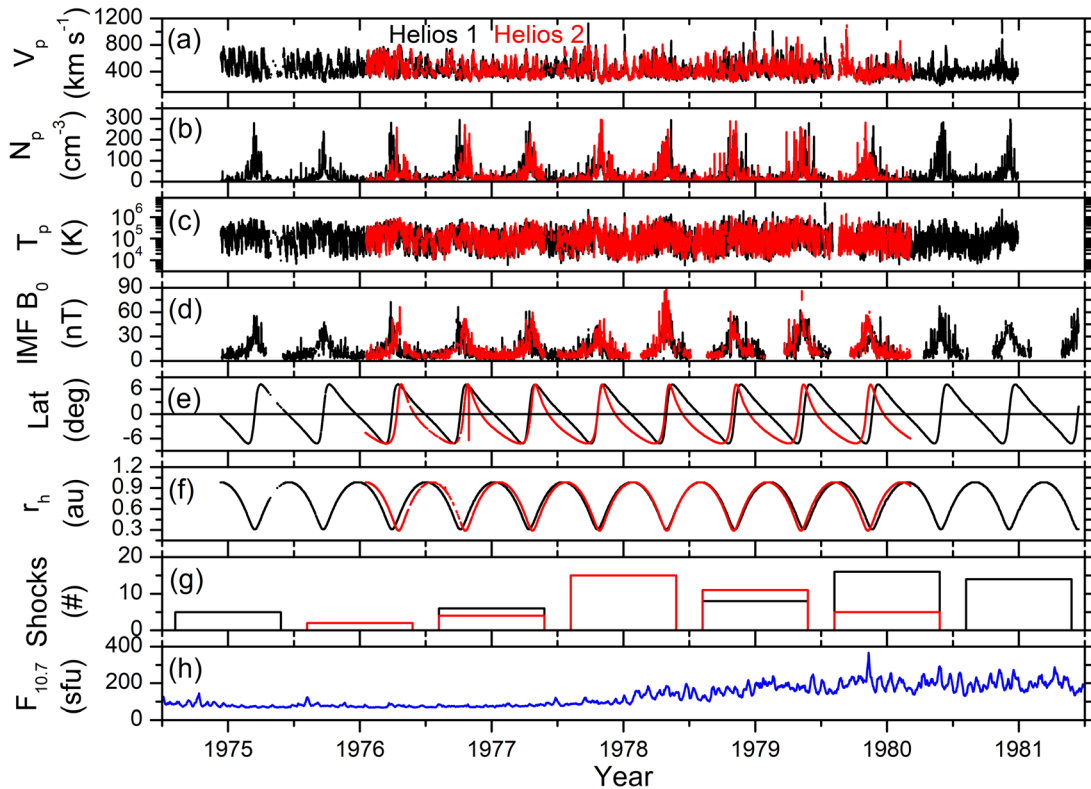


Figure 1. Overview of solar wind measurements by Helios 1 (H1, black) and Helios 2 (H2, red). From top to bottom, the panels show (a) solar wind proton speed (V_p), (b) density (N_p), (c) temperature (T_p), (d) IMF magnitude (B_0), (e) heliographic latitude, (f) heliocentric distance (r_h), (g) number of interplanetary fast forward shocks, and (h) $F_{10.7}$ solar flux. The resolution of Helios data shown (panels (a)–(f)) is 1 hr, that of shock identification (panel (g)) is 1 yr, and that of the $F_{10.7}$ solar flux (panel (h)) is 1 day.

interaction regions (CIRs: Pizzo 1985; Balogh et al. 1999). At distances beyond ~ 2.5 au from the Sun, CIRs typically are bounded by a forward shock at its antisolar edge and by a reverse shock at its solar edge (Smith & Wolfe 1976). Although CIR shocks are known to accelerate SEPs at large distances from the Sun (McDonald et al. 1975; Van Hollebeke et al. 1975; Barnes & Simpson 1976; Pesses et al. 1978, 1979; Tsurutani et al. 1985), CIRs are known to typically not have forward and reverse magnetosonic shocks at their boundaries at ~ 1.0 au from the Sun (Smith & Wolfe 1976; Tsurutani et al. 1995a, 1995b; Hajra 2021).

It is the purpose of this paper to study the IMF and plasma data from ~ 0.3 to ~ 1.0 au using the Helios 1 (H1) and Helios 2 (H2) observations to identify fast forward (FF) and fast reverse (FR) shocks using the Abraham-Shrauner (1972) technique and the Rankine–Hugoniot (Rankine 1870; Hugoniot 1887, 1889) conservation laws for shock identification.

2. Data Analysis and Results

2.1. Interplanetary Parameters

The H1 and H2 spacecraft provided in situ solar wind plasma and IMF measurements for the periods from 1974 December 30 through 1985 September 4, and from 1976 January 17 through 1980 March 8, respectively. Note that data from both spacecraft are not available over identical periods of time. This will be apparent in the results section. Figure 1 shows an overview of the measurements, namely, the solar wind proton speed (V_p), density (N_p), temperature (T_p), and IMF magnitude (B_0), followed by the heliographic latitude and heliocentric radial distance (r_h) of the spacecraft. The spacecraft location is

given in the heliographic inertial (HGI) coordinate system. The HGI coordinates are Sun-centered and inertially fixed with respect to an x -axis directed along the intersection line of the ecliptic and solar equatorial planes. The latter defines zero degree longitude. The z -axis is directed perpendicular to and northward of the solar equator, and the y -axis completes the right-hand system. The latitude span of the two spacecraft is $\sim \pm 7^\circ$ (Figure 1(e)). The spacecraft r_h ranges from 0.31 to 0.98 au for H1 and from 0.29 to 0.98 au for H2 (Figure 1(f)). These 1 hr resolution data are collected from NASA’s Space Physics Data Facility.⁸

High-time-resolution IMF and plasma data were also used in our analyses. For identification and analysis of shocks and their interplanetary drivers, 40 s average data were used.

Based on the H1 and H2 observations, distributions of the solar wind parameters are plotted at each 0.1 au (Figure 2). The median values of the parameters at different r_h values are superposed as black curves. While V_p varies slowly with r_h , larger variations are prominent for N_p , T_p , and B_0 . This is explored further in Figure 3 showing the variations of the mean values of the parameters along with their statistical trends with varying r_h . The statistical curve fitting analysis results are summarized in Table 1.

From Figures 2(a)–(b) and 3(a) and Table 1, V_p exhibits a slow increase as a function of r_h at a rate of ~ 34 – 40 km s^{-1} au^{-1} . However, a large scatter in data is reflected in an insignificant correlation (correlation coefficient $r = 0.34$ and 0.49 for H1 and H2, respectively) between V_p and r_h (Table 1). N_p , T_p , and IMF B_0 have strong dependences on r_h . With

⁸ <https://spdf.gsfc.nasa.gov/>

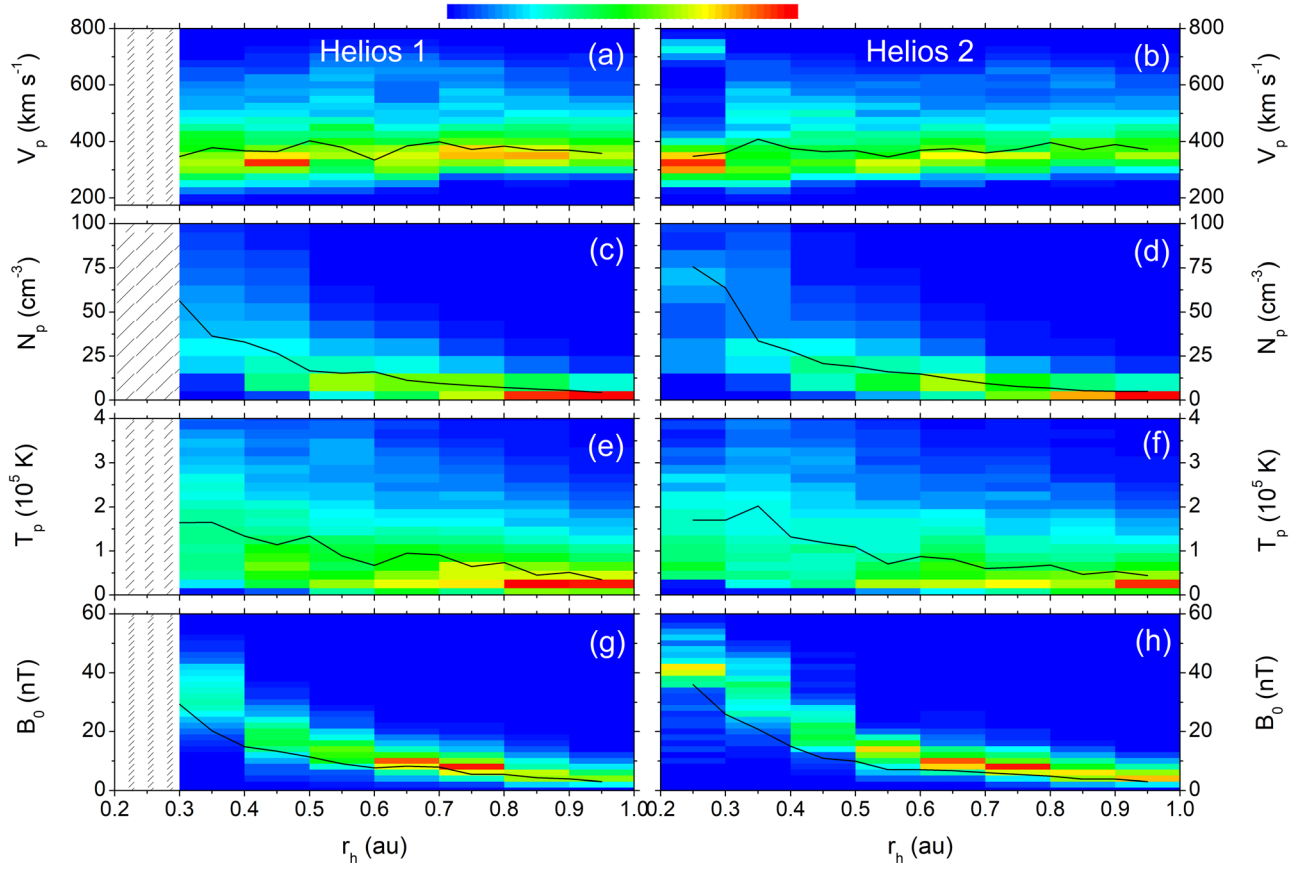


Figure 2. Distributions of the solar wind parameters as observed by H1 (left panels) and H2 (right panels). From top to bottom, the panels show distributions of (a)–(b) V_p , (c)–(d) N_p , (e)–(f) T_p , and (g)–(h) IMF B_0 as functions of r_h . Colors from blue to red indicate normalized observations in relative units designed for each graph (the color bar is at the top). Median values of the parameters at each r_h value are shown by bold black curves in the panels.

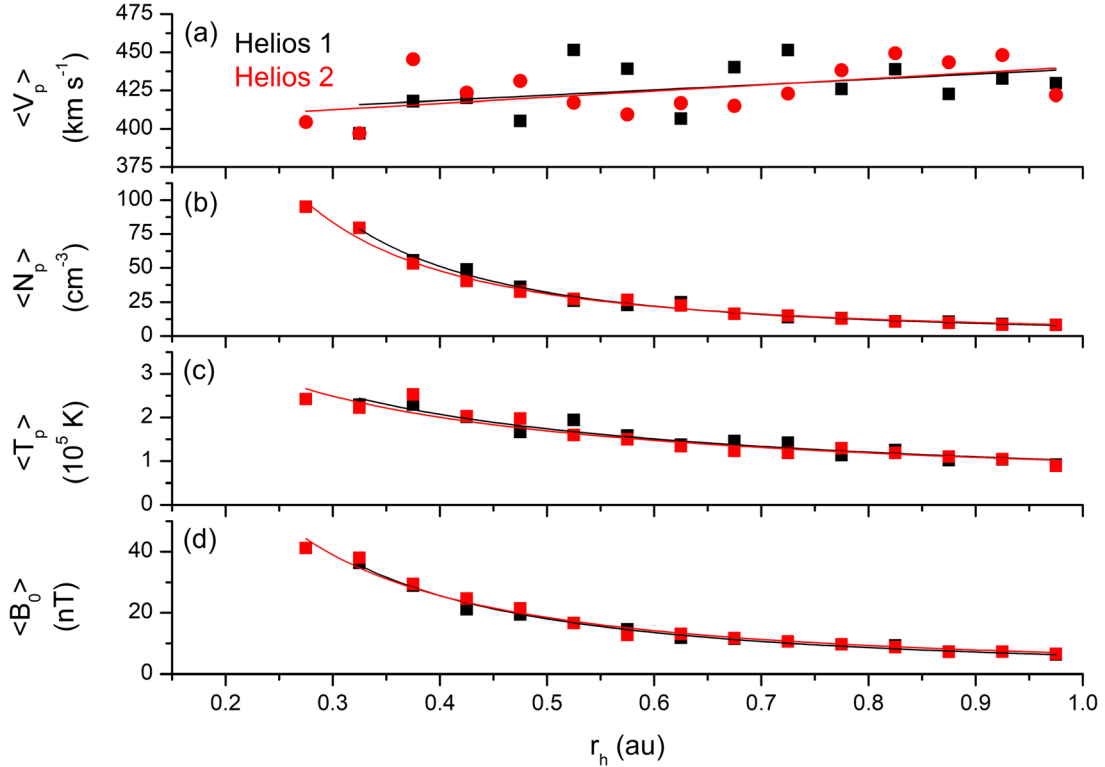


Figure 3. Variations of average solar wind parameters (a) V_p , (b) N_p , (c) T_p , and (d) B_0 with r_h . The black and red data points correspond to the H1 and H2 observations, respectively. The curve fittings are shown by solid lines. See Table 1 for details.

Table 1
Relationships of the Mean Solar Wind Parameters with r_h

| Relationship | Correlation Coefficient (r) | Confidence Level (c) |
|--|---------------------------------|--------------------------|
| $\langle V_p \rangle_{H1} = (405 \pm 14) + (34 \pm 21)r_h$ | +0.34 | >70% |
| $\langle V_p \rangle_{H2} = (401 \pm 11) + (40 \pm 17)r_h$ | +0.49 | >90% |
| $\langle N_p \rangle_{H1} = (7.63 \pm 0.50)r_h^{-2.08 \pm 0.07}$ | -1.00 | >99% |
| $\langle N_p \rangle_{H2} = (8.16 \pm 0.58)r_h^{-1.93 \pm 0.07}$ | -0.99 | >99% |
| $\langle T_p \rangle_{H1} = (1.01 \pm 0.05)r_h^{-0.78 \pm 0.06}$ | -0.96 | >99% |
| $\langle T_p \rangle_{H2} = (1.00 \pm 0.06)r_h^{-0.75 \pm 0.07}$ | -0.95 | >99% |
| $\langle B_0 \rangle_{H1} = (6.05 \pm 0.24)r_h^{-1.58 \pm 0.04}$ | -1.00 | >99% |
| $\langle B_0 \rangle_{H2} = (6.70 \pm 0.41)r_h^{-1.46 \pm 0.06}$ | -0.99 | >99% |

Note. Units of the solar wind parameters are km s^{-1} (V_p), cm^{-3} (N_p), 10^5 K (T_p), and nT (B_0); r_h is given in au.

increasing r_h , the power law decrease in N_p (r_h^{-2}) is sharper than in B_0 ($r_h^{-1.5}$) and in T_p ($r_h^{-0.8}$). The (anti)correlation coefficients (r) are ≥ 0.95 —highly significant at >99% confidence level (Table 1). These results are in general agreement with existing studies of the solar wind radial variations (e.g., Mariani et al. 1978; Bougeret et al. 1984; Hellinger et al. 2011; Marsch 2012; Hellinger et al. 2013; Venzmer & Bothmer 2018, and references therein).

2.2. Interplanetary Shocks

Potential interplanetary shocks are identified first manually by observations of the temporal variations of the solar wind plasma and IMF. The abrupt increases in V_p with simultaneous increases or decreases in N_p , T_p , and B_0 are identified as possible FF or FR shocks, respectively. The plasma and magnetic field mixed-mode technique (Abraham-Shrauner 1972; Abraham-Shrauner & Yun 1976) is applied to determine the shock normal vector, its propagation angle (θ_{Bn}) with respect to the upstream IMF vector, the speed of propagation (V_{sh}), and the magnetosonic Mach number (M_{ms}) of the potential shocks. Only those with values $M_{ms} > 1$ were confirmed as shocks. During ~ 1975 –1981, H1 and H2 encountered 68 and 39 shocks, respectively (Figure 1(g)). Among these 107 shocks, only 4 are FR shocks and the rest are FF shocks. Appendix Table A1 lists all the shocks, their drivers, and their characteristic parameters. The interval of study spans from the minimum to the maximum of the solar cycle 21, as can be seen from the variation of the $F_{10.7}$ solar flux (Figure 1(h)). The daily $F_{10.7}$ solar fluxes are obtained from the Laboratory for Atmospheric and Space Physics (LASP) Interactive Solar Irradiance Data Center.⁹

2.3. Case Studies of Interplanetary Shocks

Figure 4 shows an interplanetary shock and its driver, detected by the two spacecraft at two different distances from the Sun. The IMF data are in the spacecraft-centered radial tangential normal (RTN) coordinate system, where \hat{R} is the unit vector directed from the Sun to the spacecraft, and $\hat{T} = \Omega \times \hat{R} / |\Omega \times \hat{R}|$, where Ω is the Sun’s spin axis. The right-hand system is completed by \hat{N} .

The FF shock was encountered by H1 and H2 at $\sim 11:33$ UT and $\sim 19:47$ UT (on day 75 of 1977), respectively. The spacecraft were at r_h of 0.61 au and 6.6° S heliographic latitude

(H1), and at r_h of 0.72 au and 7.2° S heliographic latitude (H2). At the H1 (H2) location, the shock is characterized by sharp increases in V_p from ~ 309 to ~ 366 km s^{-1} (from ~ 321 to ~ 388 km s^{-1}), in N_p from ~ 41 to ~ 88 cm^{-3} (from ~ 14 to ~ 36 cm^{-3}), in T_p from $\sim 1.03 \times 10^5$ to $\sim 2.20 \times 10^5$ K (from $\sim 0.36 \times 10^5$ to $\sim 0.75 \times 10^5$ K), and in IMF B_0 from ~ 14 to ~ 18 nT (from ~ 7 to ~ 14 nT). From the H1 (H2) measurements, the shock is found to propagate at a speed V_{sh} of ~ 404 km s^{-1} (~ 398 km s^{-1}) at a normal angle θ_{Bn} of $\sim 21^\circ$ ($\sim 29^\circ$) relative to the ambient IMF. Thus, the shock is quasi-parallel ($\theta_{Bn} < 45^\circ$). From the H1 measurements, the computed shock M_{ms} is ~ 1.6 , and compressions in plasma N_p and IMF B_0 between the solar winds downstream to upstream of the shock are ~ 2.2 and ~ 1.3 , respectively. At H2, M_{ms} is ~ 1.8 , and the N_p and B_0 compressions are ~ 2.4 and ~ 1.9 , respectively. It is noted that although the same shock was detected at a distance of only 0.11 au apart, the shock normal angles and compression ratios were different. This is primarily due to the differences in the upstream parameters. For instance, at H1, the upstream IMF cone angle (with respect to the Sun–spacecraft line) varied between $\sim 26^\circ$ and $\sim 41^\circ$, with an average cone angle of $\sim 35^\circ$. At H2, the upstream IMF cone angle varied between $\sim 36^\circ$ and $\sim 86^\circ$, with an average value of $\sim 61^\circ$.

Downstream of the shock is a region with compressed plasma and largely fluctuating IMF, known as the interplanetary sheath. The sheath signatures are noted from $\sim 11:33$ UT to $\sim 16:48$ UT on day 75 in the H1 measurements, and from $\sim 19:47$ UT on day 75 to $\sim 03:20$ UT on day 76 in the H2 measurements. The sheath at H1 (H2) is characterized by high values of $N_p \sim 96$ cm^{-3} (~ 87 cm^{-3}), $T_p \sim 1.78 \times 10^5$ K ($\sim 1.33 \times 10^5$ K), and $B_0 \sim 28$ nT (~ 21 nT).

The region after the interplanetary sheath (shaded regions, from $\sim 16:48$ UT on day 75 to $\sim 07:38$ UT on day 77 for H1, and from $\sim 03:20$ UT on day 76 to $\sim 12:47$ UT on day 77 for H2) is characterized by a slow decrease in V_p , a low N_p , a low T_p , and smooth rotations in the IMF components. These are the typical signatures of a magnetic cloud, which is one part of an ICME (Burlaga et al. 1981; Tsurutani et al. 1988; Burlaga et al. 1998; Tsurutani et al. 1998).

From the above information and detailed high-time-resolution shock analyses, the discontinuity was classified as an ICME-driven FF shock.

The interplanetary event shown in Figure 5 represents an interaction between a slow stream with plasma V_p of ~ 430 km s^{-1} on day 82 and an HSS with peak V_p of ~ 770 km s^{-1} on day 84 of 1978. This was identified by H2 at $r_h \sim 0.71$ au and heliographic latitude of $\sim 7.2^\circ$ S. The interaction region, which can be noted between $\sim 04:16$ UT and $\sim 13:47$ UT on day 83 (shaded region), is characterized by an enhanced N_p of ~ 97 cm^{-3} and an enhanced B_0 of ~ 35 nT. This is identified as a CIR. The CIR trailing edge is characterized by a sharp increase in V_p from ~ 620 to ~ 669 km s^{-1} and a simultaneous decrease in N_p from ~ 19 to ~ 10 cm^{-3} , a decrease in T_p from $\sim 4.90 \times 10^5$ to $\sim 3.30 \times 10^5$ K, and a decrease in B_0 from ~ 21 to ~ 15 nT. The shock M_{ms} is estimated to be ~ 1.8 , speed V_{sh} is ~ 124 km s^{-1} , and propagation angle θ_{Bn} is $\sim 56^\circ$ (a quasi-perpendicular shock with $\theta_{Bn} \geq 45^\circ$). This is a CIR-driven FR shock. Another discontinuity is identified inside the CIR at $\sim 09:36$ UT on day 83 (vertical black solid line). This is characterized by a slow increase in V_p (440 – 520 km s^{-1}), a sharp fall in N_p (91 – 22 cm^{-3}), and a simultaneous sharp increase in T_p (1.40×10^5 – 7.19×10^5 K). This discontinuity

⁹ <https://lasp.colorado.edu/lisird/>

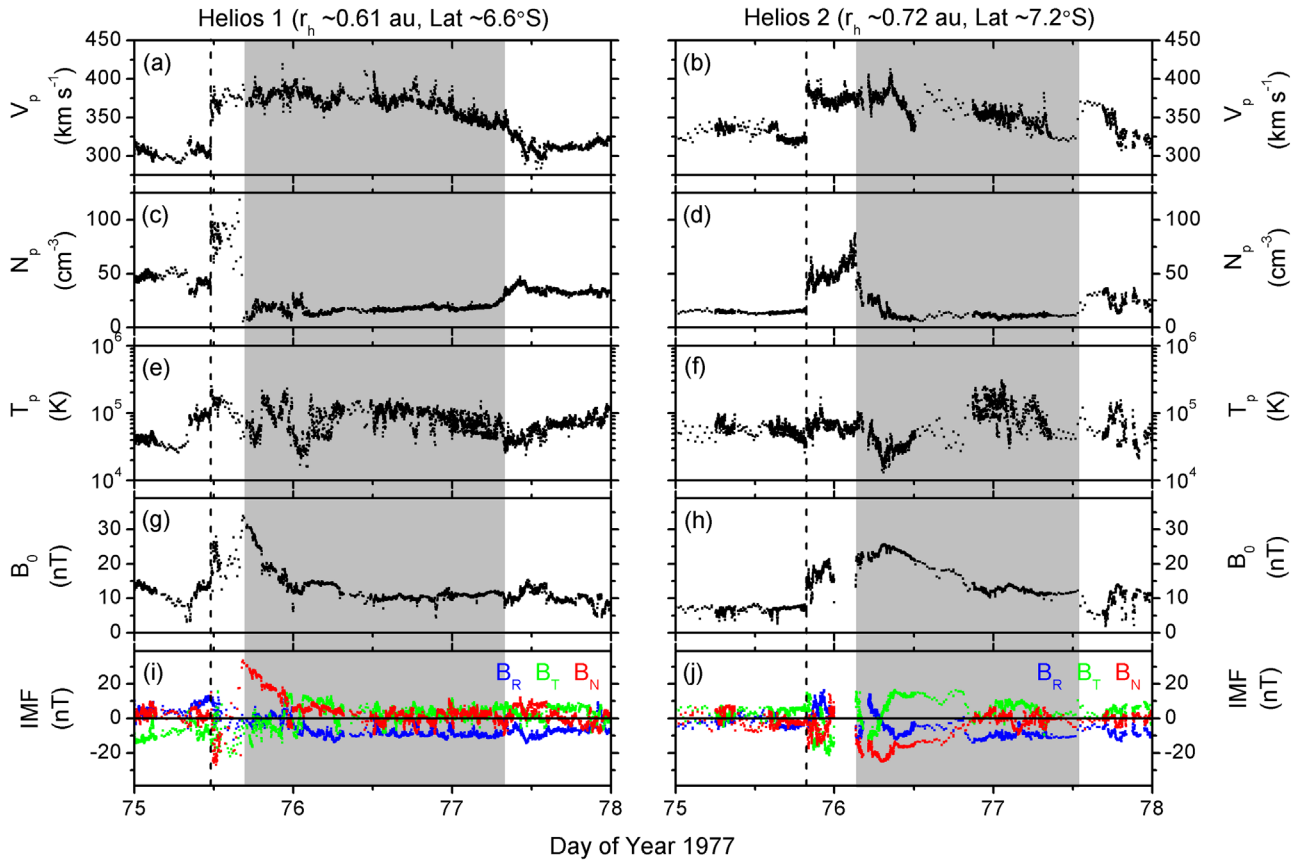


Figure 4. An interplanetary shock driven by an ICME, detected by both H1 (left) and H2 (right) during days 75–77 of 1977. From top to bottom, the panels show (a)–(b) V_p , (c)–(d) N_p , (e)–(f) T_p , (g)–(h) IMF B_0 , and (i)–(j) IMF components B_R , B_T , and B_N . The dashed vertical lines indicate the shock encounter times at the two spacecraft. The shaded regions show a magnetic cloud.

separating a cold, dense plasma from a hot, low-density plasma is called a stream interface (SI). The SI is a tangential discontinuity that separates the compressed slow solar wind plasma and magnetic fields from the compressed fast solar wind plasma and magnetic fields. It should be noted that at the CIR leading edge, there is no FF shock. Previous studies done at 1 au have noted that CIRs sometimes have FR shocks with no FF shocks (e.g., Belcher & Davis 1971; Tsurutani et al. 1995a; Jian et al. 2006; Hajra & Sunny 2022, and references therein).

2.4. Statistical Properties of Interplanetary Shocks

The yearly number of FF shocks was previously shown in Figure 1(g). The FF shocks exhibited a clear correlation with the $F_{10.7}$ solar flux (Figure 1(h)). The correlation coefficient between the yearly shock number and the yearly mean $F_{10.7}$ solar flux is $r = 0.65$ (significant at $>80\%$ confidence level). In Figure 6, distributions of the FF shocks as a function of heliographic latitude and r_h are studied. The FR shocks are excluded from these statistics as they are significantly different in properties compared to the FF shocks. Due to the low number (four) of FR shocks, no separate statistics for them were derived.

The total number of shocks identified by the two spacecraft exhibits an exponential increase with the increasing radial distance from the Sun (Figure 6(c)). However, this observation can be due to either varying spacecraft observation times or varying $F_{10.7}$ solar flux, or both. Thus, the FF shock occurrences are normalized with respect to the observation

period and the $F_{10.7}$ solar flux. The results of these two normalization factors are shown in Figure 6(d). The FF shocks normalized by the observation period at each 0.1 au r_h sector (blue histograms, Figure 6(d)) do not exhibit any obvious relationship with r_h . However, the shock normalized by both factors (empty histograms, Figure 6(d)) exhibits a correlation coefficient $r = 0.76$ with r_h , significant at a $>95\%$ confidence level. One speculation is that the number of shocks increases primarily with the increasing $F_{10.7}$ solar flux (Figure 1(g)) and secondarily with the increasing r_h (Figure 6(d)).

All shocks identified in this work are classified as ICME-driven or CIR-driven shocks (examples were shown in Figures 4 and 5). The four FR shocks are associated with CIRs. Among the 103 FF shocks identified in this work, 91 (88%) are found to be driven by ICMEs, and 12 (12%) by CIRs.

The two spacecraft encountered more than 73 HSSs during the period of this study. CIRs or proto-CIRs were identified in each case. However, only 16 ($\sim 22\%$) of the CIRs/proto-CIRs formed interplanetary shocks between 0.29 and 0.98 au.

The distributions of the ICME- and CIR-driven FF shocks are shown in Figure 7. While the ICME shocks are observed throughout the inner heliosphere, only a few CIR shocks are found to develop after 0.35 au from the Sun.

It is surprising to note from Figure 7 that most of the CIR shocks are formed at r_h of 0.35 to 0.55 au. This is in contrast to the present understanding (as mentioned before) that the CIR shocks rarely form at $r_h \leq 1.0$ au (Smith & Wolfe 1976; Tsurutani et al. 1995a, 1995b; Hajra 2021). We have looked to

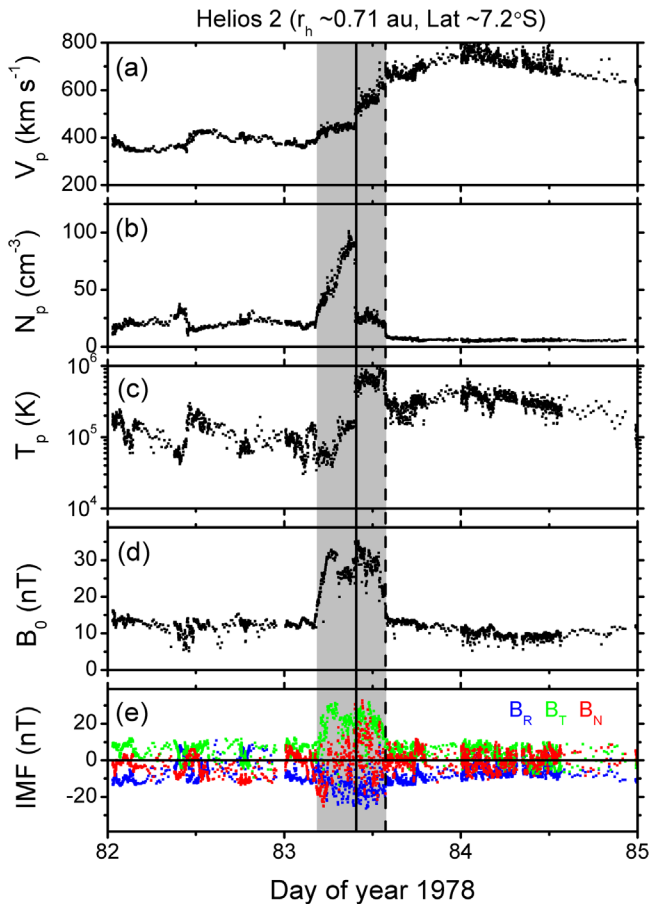


Figure 5. A CIR (shading) identified on day 83 of 1978. An HSS is to the right of the shading and a slow stream to the left of the shading. The panels are in the same format as in Figure 4. The dashed vertical line indicates a fast reverse shock. The solid vertical line indicates a stream interface.

see if there were unusual features of either the HSS or the upstream slow-speed stream that led to shock formation. However, no obvious distinguishing features were noted between CIRs with and without shocks.

For each of the shocks identified, we estimated the shock parameters, such as the shock normal angles θ_{Bn} , with respect to the upstream IMF, the shock propagation speeds V_{sh} , and the shock magnetosonic Mach numbers M_{ms} . The shock jump conditions are also given, namely the shock compressions in IMF B_0 and N_p (or the B_0 and the N_p jump ratios) between the solar wind downstream and upstream values. The radial variations of the statistical means (and standard deviations) of the FF shock parameters are shown in Figure 8. For comparison, the FR shock parameters are shown by blue crosses in the same figure. While the FR shock speeds are significantly lower than the mean speeds of the FF shocks at any radial distance (Figure 8(b)), no significant differences could be inferred in other shock parameters. The relationships of the FF shock parameters with r_h are studied by linear regression analysis and with the computation of the correlation coefficient (r) and corresponding confidence level (c), which are listed in Table 2. From the figure, it can be concluded that the FF shock strength (as depicted by the shock M_{ms} and by the B_0 and N_p jump ratios) exhibits a clear increasing trend with increasing radial distance from the Sun. The increase rate of M_{ms} is $\sim 0.7 \text{ au}^{-1}$, that of B_0 jump is $\sim 0.89 \text{ au}^{-1}$, and that of N_p jump is $\sim 0.98 \text{ au}^{-1}$. The relationships are statistically

confirmed by high correlation coefficients $r \geq 0.63$, significant at high confidence levels $c > 90\%$. There are no r_h dependences of the shock normal angle (θ_{Bn}) and speed (V_{sh}).

Figure 9 shows the distributions of the FF shock parameters observed throughout the inner heliosphere. Large ranges of the parameter values are clear from the figure. The statistical features of the parameters are summarized in Table 3.

M_{ms} ranged from 1.03 to 6.42, with an average M_{ms} of ~ 1.91 for all FF shocks. V_{sh} varied from 181 to 902 km s^{-1} , with an average V_{sh} of $\sim 515 \text{ km s}^{-1}$. θ_{Bn} ranged from $\sim 6^\circ$ to $\sim 90^\circ$, with two peaks around 40° and 80° . The IMF B_0 and plasma N_p compressions ranged from 1.21 to 5.41 and 1.23 to 4.46, with average B_0 and N_p compressions of ~ 2.00 and ~ 2.06 , respectively.

According to the magnetohydrodynamic (MHD) theory of Kennel et al. (1985), for noncritical quasi-perpendicular shocks, the approximate jump ratios of IMF B_0 and N_p should be close to the Mach number up to a value of ~ 4.0 . Here we note that the mean M_{ms} (~ 1.91) is slightly less than 2.0 and the IMF compression (~ 2.00) and plasma compression (~ 2.06) are about the same, which is in general agreement with the MHD theory.

Among all ICME FF shocks (CIR FF shocks), 60% (75%) are quasi-perpendicular, and 40% (25%) are quasi-parallel (not shown). Among the four FR shocks identified in this work, three are quasi-perpendicular, and one is quasi-parallel. It is interesting to note from Table 2 that the ICME- and CIR-driven FF shocks do not exhibit any (statistically) significant differences in the shock parameters, except that the ICME shocks are significantly faster ($\sim 20\%$) with higher M_{ms} ($\sim 28\%$) than the CIR shocks, on average.

2.5. Shocks Identified by Both Spacecraft

Among the shocks studied in this work, 17 were identified by both spacecraft separated by some distance. Figure 10 shows a comparison of the FF shock parameters as identified by the two spacecraft. From this analysis, no correlation can be inferred between the shock parameters at the two locations.

3. Summary and Discussion

From the H1 and H2 solar wind measurements between ~ 0.3 and 1.0 au heliocentric distance, a total of 107 fast interplanetary shocks (with $M_{\text{ms}} > 1$) are identified. Among them, only 4 are FR shocks, and 103 are FF shocks. The following results are obtained from the detailed analysis of the shocks:

1. The normalized number of shocks increases with increasing solar $F_{10.7}$ flux, and with increasing heliocentric distance r_h .
2. The FF shock normal angle θ_{Bn} ranged from $\sim 6^\circ$ to $\sim 90^\circ$, with an average θ_{Bn} of $\sim 56^\circ$ for all FF shocks. θ_{Bn} is found to be independent of r_h , which is surprising.
3. Among all ICME FF shocks (CIR FF shocks), 60% (75%) are quasi-perpendicular ($\theta_{\text{Bn}} \geq 45^\circ$), and 40% (25%) are quasi-parallel ($\theta_{\text{Bn}} < 45^\circ$).
4. When the shock was detected at both H1 and H2 spacecraft there was no strong correlation of either the shock normal angles, Mach numbers, or shock speeds. Part of this was due to the difference in upstream

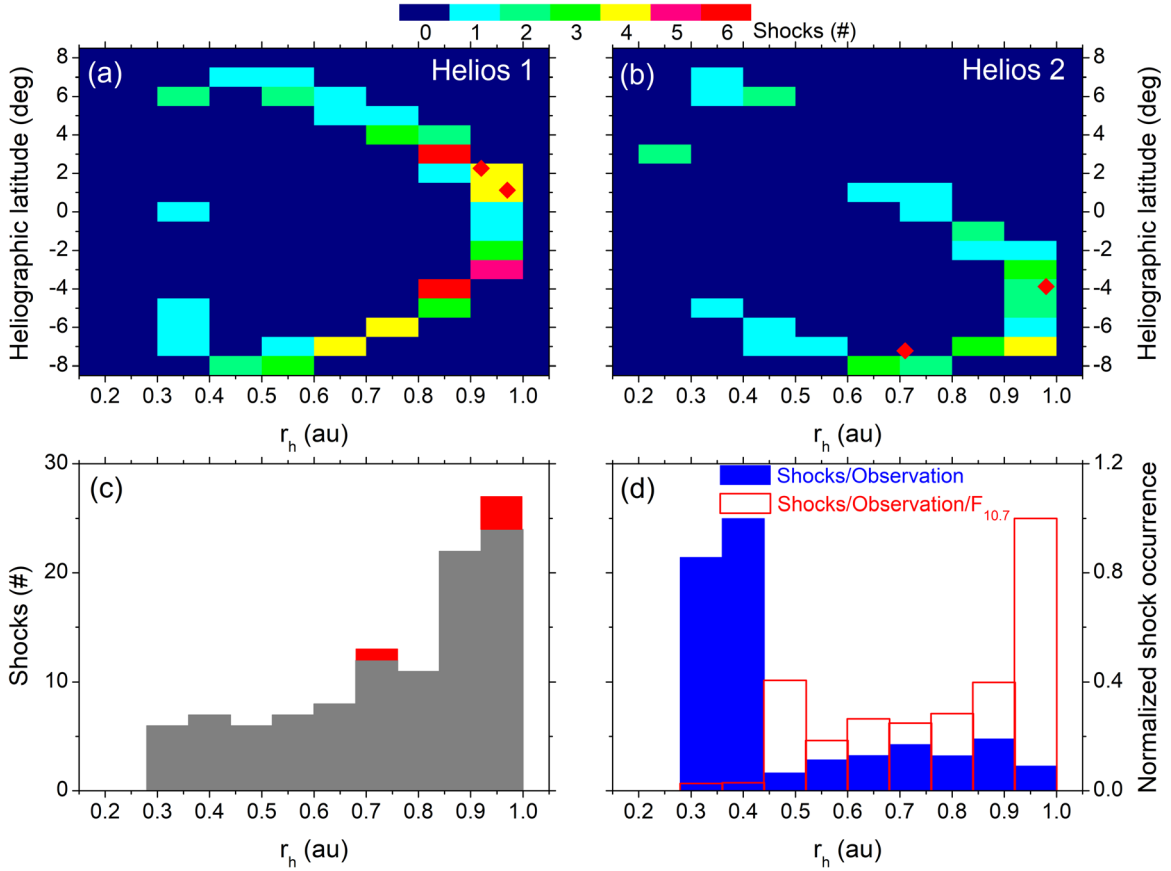


Figure 6. Shock distributions. The top panels are contour plots of FF shocks identified by (a) H1 and (b) H2 as a function of heliographic latitude and r_h . The numbers of shocks are indicated by the color bar at the top. Locations of four FR shocks are marked by red diamonds. The bottom panels are (c) the total number of H1 and H2 FF shocks detected as a function of r_h , and (d) the normalized shock occurrences as functions of r_h . In panel (c) FR shocks are indicated in red.

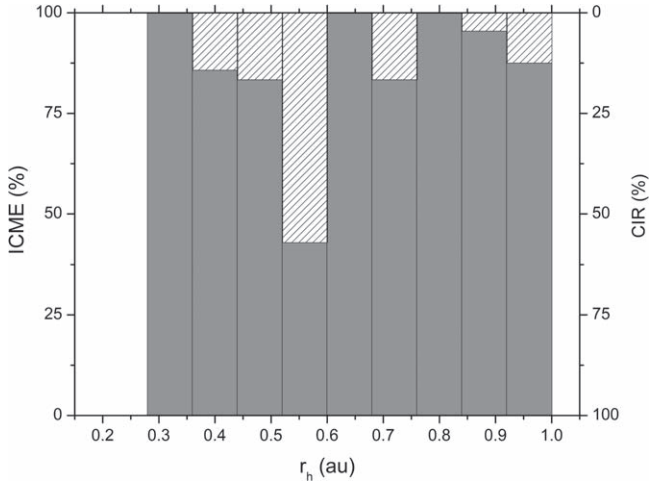


Figure 7. Shock drivers. Percentages of the FF shocks driven by ICMEs (gray, scale on the left) and CIRs (hatching, scale on the right) as a function of r_h .

magnetic field directions, upstream plasma densities, and magnetic field strengths.

5. The FF shock Mach number M_{ms} ranged from 1.03 to 6.42. The mean value is ~ 1.91 . M_{ms} increases with r_h at a rate of $\sim 0.7 \text{ au}^{-1}$. The radial relationship of M_{ms} is confirmed by the linear correlation coefficient $r = 0.63$, significant at a confidence level $> 90\%$.

6. The FF shock speed V_{sh} ranged from a minimum value of 181 km s^{-1} to a maximum value of 902 km s^{-1} . It is found to be independent of r_h .
7. Among all FF shocks, 88% were found to be driven by ICMEs. Only 12% of the FF shocks were driven by CIRs (those detected within 0.35 and 0.55 au).
8. The mean FF shock M_{ms} (~ 1.91) and plasma compression ratio (~ 2.06) have values that are essentially the same, which is in agreement with the MHD theory (Kennel et al. 1985).
9. With the increasing r_h , the average solar wind plasma speed is found to increase slowly at $\sim 34\text{--}40 \text{ km s}^{-1} \text{ au}^{-1}$, while the average density exhibits a sharper fall (r_h^{-2}) compared to the magnetic field magnitude ($r_h^{-1.5}$) and the temperature ($r_h^{-0.8}$).

The most surprising result of this study is that the statistical shock normal angle is not quasi-parallel at H1 and H2 orbits closest to the Sun (~ 0.3 au). The shock normal angle is a more or less constant $\sim 56^\circ$ from ~ 0.3 to 0.98 au (Figure 8). This indicates that the ICME shock properties are highly influenced by upstream discontinuities or upstream Alfvén waves, or that the shocks themselves have wavy structures. Of course, all three possibilities may be occurring as well.

Figure 8 gives the FF shock parameters as a function of r_h from ~ 0.3 to 1.0 au. The shock occurrence, M_{ms} , and plasma and magnetic compressions show increasing trends with increasing r_h and are highly correlated to r_h (correlation coefficient r between 0.63 and 0.83). These results can be

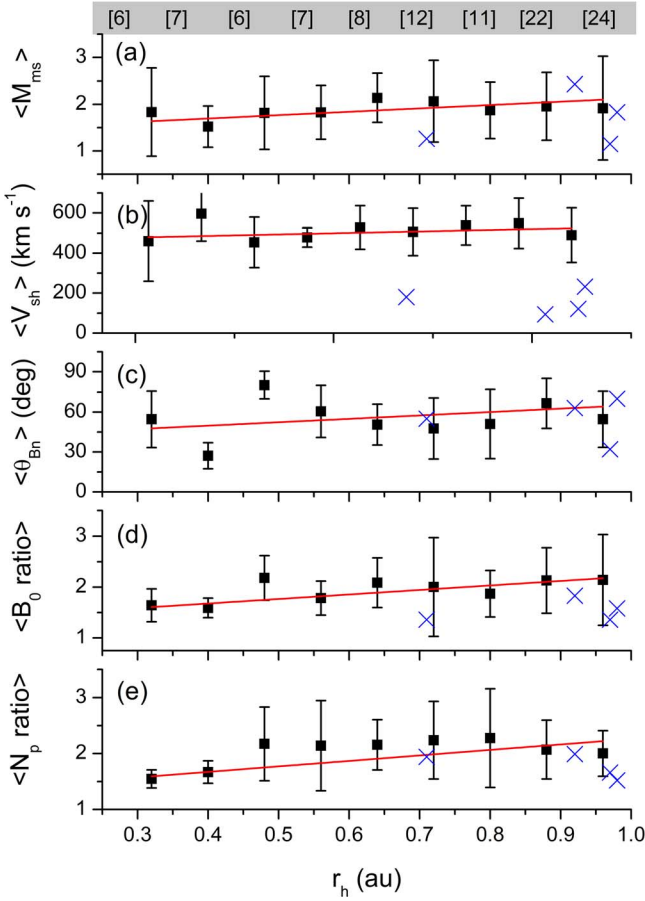


Figure 8. Variations of the mean FF shock parameters (a) $\langle M_{\text{ms}} \rangle$, (b) $\langle V_{\text{sh}} \rangle$, (c) $\langle \theta_{\text{Bn}} \rangle$, (d) $\langle B_0 \text{ ratio} \rangle$, and (e) $\langle N_p \text{ ratio} \rangle$ with r_h . Vertical bars show the standard deviations from the mean values. The regression lines are shown in each panel. See Table 2 for details. Numbers at the top represent the FF shock numbers in each r_h bin. Blue crosses in each panel correspond to the FR shock parameters.

Table 2
Relationships of the Mean FF Shock Parameters with r_h

| Relationship | Correlation Coefficient (r) | Confidence Level (c) |
|--|---------------------------------|--------------------------|
| $\langle M_{\text{ms}} \rangle = (1.41 \pm 0.21) + (0.72 \pm 0.34)r_h$ | 0.63 | >90% |
| $\langle V_{\text{sh}} \rangle = (457 \pm 55) + (70 \pm 86)r_h$ | 0.29 | >0% |
| $\langle \theta_{\text{Bn}} \rangle = (40 \pm 23) + (26 \pm 40)r_h$ | 0.24 | >0% |
| $\langle B_0 \text{ ratio} \rangle = (1.32 \pm 0.18) + (0.89 \pm 0.35)r_h$ | 0.70 | >95% |
| $\langle N_p \text{ ratio} \rangle = (1.28 \pm 0.12) + (0.98 \pm 0.25)r_h$ | 0.83 | >99% |

Note. V_{sh} is given in km s^{-1} , θ_{Bn} in degrees, and r_h in au.

compared with the radial variations of shock parameters in the outer heliosphere, beyond ~ 1.0 au from the Sun. The shock occurrence is found to peak at ~ 5.0 au (e.g., Hoang et al. 1995; González-Esparza et al. 1998; Richardson & Wang 2005; Neugebauer 2013; Echer 2019), beyond which it decreases linearly (Hajra 2021). In addition, Hajra (2021) reported that the radial variation of the shock M_{ms} between ~ 1.0 and ~ 15.0 au is slower and less correlated to r_h .

The results could be useful for modelers (Zank et al. 2006; Verkhoglyadova et al. 2010) who wish to investigate the SEP acceleration for a shock propagating from the Sun to ~ 1.0 au and beyond. Both the solar wind and shock properties change

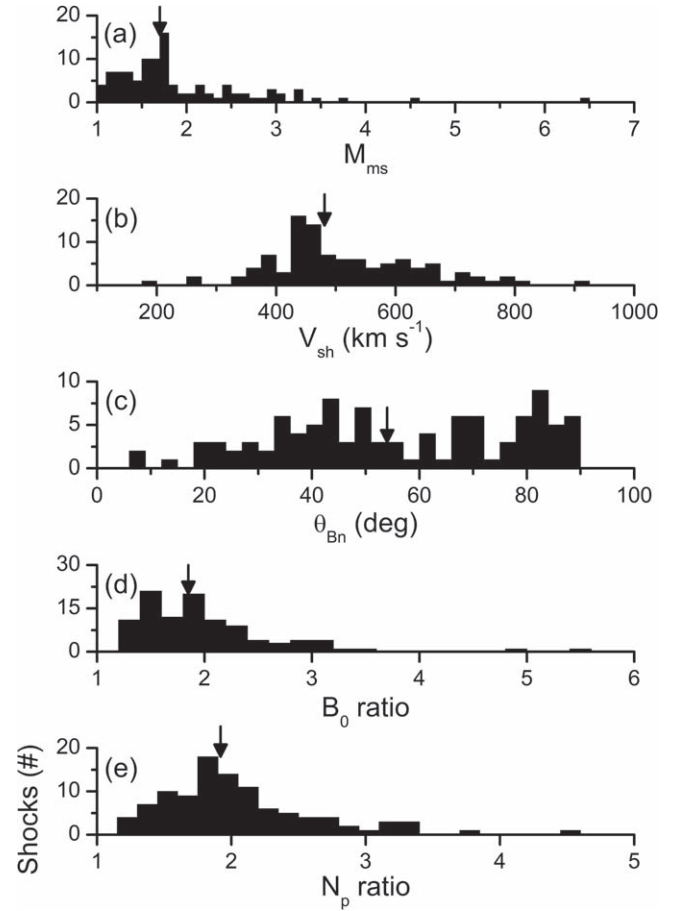


Figure 9. Histograms of the FF shock parameters (a) M_{ms} , (b) V_{sh} , (c) θ_{Bn} , (d) IMF B_0 jump ratio, and (e) N_p jump ratio for all FF shocks. The arrow pointing downward in each panel indicates the median values.

as a function of radial distances and, by encoding the changes in incremental r_h steps, a more accurate representation will be obtained.

4. Final Comments

Although this paper discusses the general features of solar wind plasma and magnetic fields between ~ 0.3 and ~ 1.0 au, we have not examined the ion distribution functions as Marsch et al. (1982a, 1982b) did in some detail. The latter authors have noted that the ion distribution functions at all H1 and H2 radial distances have $T_{\perp}/T_{\parallel} > 1$. With an expanding solar wind with decreasing magnetic field strengths and increasing distance from the Sun, the conservation of the first adiabatic invariant should lead to ion beaming ($T_{\parallel}/T_{\perp} > 1$). But how can the ions attain $T_{\perp}/T_{\parallel} > 1$ anisotropies? One possibility is that the ponderomotive force associated with interplanetary Alfvén waves (Tsurutani et al. 2002; Dasgupta et al. 2003; Lundin & Guglielmi 2006; Smolyakov et al. 2007) could lead to heating in T_{\perp} . Other plasma processes, based on nonlinear dynamics of large-amplitude shear Alfvén waves, could also lead to perpendicular ion heating (Khazanov et al. 1996; Sakai et al. 2005; Khazanov & Singh 2007). It would be interesting to know how microscopic processes leading to $T_{\perp}/T_{\parallel} > 1$ ion anisotropy affects the properties of interplanetary shocks.

The microphysics discussed above will affect the macro-properties of the solar wind plasma studied in this paper. For example, all of the above little-understood physical properties

Table 3
Statistical Mean \pm Standard Deviation (Median) of the FF Shock Parameters

| Shock Parameters | All FF Shocks (103) ^a | ICME FF Shocks (91) ^a | CIR FF Shocks (12) ^a |
|--|----------------------------------|----------------------------------|---------------------------------|
| M_{ms} | 1.91 ± 0.80 (1.70) | 1.96 ± 0.82 (1.72) | 1.53 ± 0.53 (1.39) |
| V_{sh} (km s^{-1}) | 515 ± 127 (481) | 525 ± 130 (513) | 439 ± 57 (450) |
| θ_{Bn} (deg) | 56 ± 22 (54) | 55 ± 23 (51) | 62 ± 20 (57) |
| B_0 jump ratio | 2.00 ± 0.68 (1.85) | 2.02 ± 0.68 (1.85) | 1.88 ± 0.66 (1.74) |
| N_p jump ratio | 2.06 ± 0.58 (1.92) | 2.07 ± 0.58 (1.92) | 1.96 ± 0.59 (1.88) |

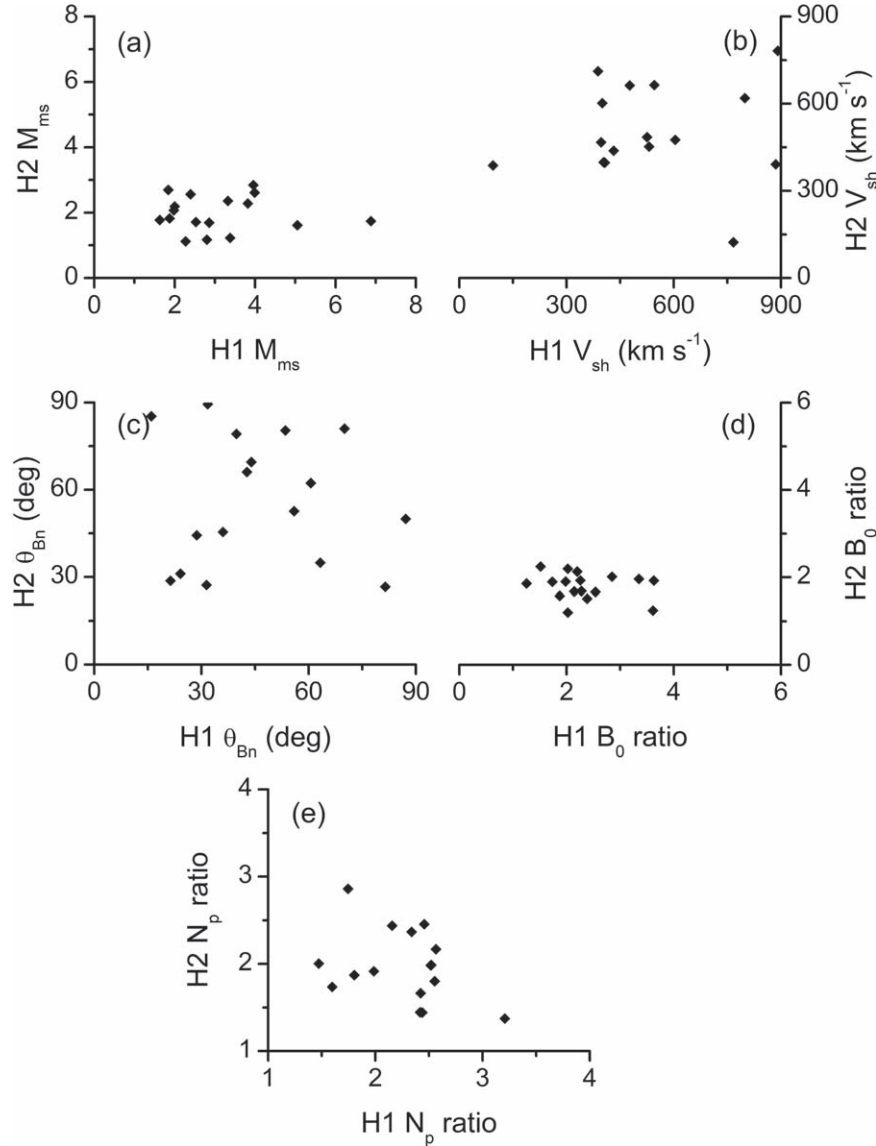
Note.^a Number of FF shocks.

Figure 10. Comparison of the FF shock parameters identified by the two spacecraft. Variations of (a) M_{ms} , (b) V_{sh} , (c) θ_{Bn} , (d) B_0 jump ratio, and (e) N_p jump ratio at H2 with those at H1 location.

may be related to solar wind plasma heating, which, in turn, will affect the solar wind velocity. Thus, the small velocity increase with increasing radial distance found in this study may be due to microphysical properties. In this sense, our current results are in support of the important findings of Marsch et al. (1982a, 1982b). Tsurutani et al. (2023) have suggested that the reconnection of interplanetary magnetic switchbacks associated with nonlinear spherical interplanetary Alfvén waves could be

another source of local solar wind heating. It will be interesting to find out whether Solar Orbiter and Parker Solar Probe scientists find similar or different sources of solar wind heating at distances closer to the Sun.

Table A1
Shocks Encountered by Helios 1 and 2

| Helios 1 Observation | | | | | | Type | Driver | Helios 2 Observation | | | | | |
|----------------------|--------------|-------------|---------------|------------|------------|-----------|------------|----------------------|--------------|-------------|---------------|------------|------------|
| Year | DOY | r_h | θ_{Bn} | V_{sh} | M_{ms} | | | Year | DOY | r_h | θ_{Bn} | V_{sh} | M_{ms} |
| 1975 | 6.86 | 0.92 | 59 | 596 | 2.7 | FF | ICME | | | | | | |
| 1975 | 8.02 | 0.92 | 56 | 703 | 2.9 | FF | ICME | | | | | | |
| 1975 | 91.55 | 0.47 | 87 | 372 | 1.8 | FF | CIR | | | | | | |
| 1975 | 325.59 | 0.89 | 79 | 437 | 1.8 | FF | ICME | | | | | | |
| 1975 | 342.17 | 0.96 | 69 | 447 | 1.5 | FF | ICME | | | | | | |
| | | | | | | FF | ICME | 1976 | 90.19 | 0.48 | 64 | 286 | 1.3 |
| | | | | | | FF | ICME | 1976 | 92.56 | 0.44 | 58 | 616 | 3.0 |
| 1976 | 272.96 | 0.34 | 82 | 235 | 1.6 | FF | ICME | | | | | | |
| 1976 | 336.70 | 0.87 | 81 | 322 | 1.6 | FF | CIR | | | | | | |
| | | | | | | FR | CIR | 1977 | 11.85 | 0.98 | 70 | 231 | 2.4 |
| 1977 | 25.62 | 0.96 | 53 | 320 | 1.1 | FF | ICME | | | | | | |
| 1977 | 75.48 | 0.61 | 21 | 404 | 1.6 | FF | ICME | 1977 | 75.82 | 0.72 | 29 | 398 | 1.8 |
| | | | | | | FF | ICME | 1977 | 83.18 | 0.64 | 29 | 477 | 1.7 |
| 1977 | 263.79 | 0.63 | 58 | 523 | 2.7 | FF | ICME | | | | | | |
| 1977 | 263.86 | 0.63 | 23 | 561 | 2.5 | FF | ICME | | | | | | |
| | | | | | | FF | CIR | 1977 | 311.79 | 0.40 | 28 | 408 | 1.5 |
| 1977 | 335.22 | 0.74 | 61 | 407 | 2.0 | FF | ICME | 1977 | 335.06 | 0.70 | 62 | 397 | 2.2 |
| 1977 | 356.85 | 0.90 | 78 | 403 | 1.7 | FF | ICME | | | | | | |
| 1978 | 1.72 | 0.94 | 86 | 424 | 1.1 | FF | ICME | | | | | | |
| 1978 | 3.36 | 0.95 | 81 | 885 | 4.0 | FF | ICME | 1978 | 3.62 | 0.94 | 27 | 391 | 2.8 |
| | | | | | | FF | ICME | 1978 | 9.84 | 0.96 | 39 | 521 | 2.1 |
| | | | | | | FF | ICME | 1978 | 37.29 | 0.98 | 27 | 448 | 2.1 |
| | | | | | | FF | ICME | 1978 | 56.20 | 0.91 | 85 | 670 | 1.1 |
| 1978 | 60.51 | 0.88 | 87 | 546 | 3.3 | FF | ICME | 1978 | 60.18 | 0.89 | 50 | 664 | 2.4 |
| 1978 | 67.36 | 0.83 | 74 | 390 | 3.0 | FF | ICME | | | | | | |
| | | | | | | FR | CIR | 1978 | 83.57 | 0.71 | 56 | 124 | 1.8 |
| | | | | | | FF | CIR | 1978 | 99.30 | 0.52 | 84 | 524 | 2.0 |
| | | | | | | FF | ICME | 1978 | 108.56 | 0.39 | 41 | 678 | 1.6 |
| | | | | | | FF | ICME | 1978 | 119.11 | 0.29 | 89 | 291 | 1.8 |
| 1978 | 119.16 | 0.31 | 36 | 767 | 5.1 | FF | ICME | 1978 | 119.12 | 0.29 | 45 | 123 | 1.6 |
| 1978 | 127.84 | 0.36 | 32 | 799 | 2.9 | FF | ICME | 1978 | 127.93 | 0.34 | 89 | 619 | 1.7 |
| 1978 | 129.40 | 0.38 | 30 | 614 | 1.7 | FF | ICME | | | | | | |
| | | | | | | FF | ICME | 1978 | 132.22 | 0.39 | 38 | 609 | 1.8 |
| | | | | | | FF | ICME | 1978 | 134.63 | 0.43 | 43 | 432 | 1.5 |
| 1978 | 268.10 | 0.75 | 77 | 557 | 2.3 | FF | CIR | | | | | | |
| 1978 | 286.57 | 0.54 | 70 | 397 | 1.6 | FF | CIR | | | | | | |
| 1978 | 291.67 | 0.47 | 74 | 479 | 1.6 | FF | ICME | | | | | | |
| 1978 | 339.74 | 0.63 | 45 | 441 | 3.5 | FF | ICME | | | | | | |
| | | | | | | FF | CIR | 1978 | 347.53 | 0.75 | 79 | 474 | 2.2 |
| 1978 | 356.38 | 0.79 | 84 | 505 | 1.4 | FF | ICME | | | | | | |
| 1978 | 356.85 | 0.80 | 44 | 604 | 2.3 | FF | ICME | 1978 | 358.34 | 0.84 | 69 | 476 | 1.1 |
| 1978 | 359.73 | 0.82 | 85 | 648 | 1.7 | FF | ICME | | | | | | |
| 1978 | 362.96 | 0.84 | 24 | 891 | 3.8 | FF | ICME | 1978 | 363.25 | 0.88 | 31 | 781 | 2.3 |
| | | | | | | FF | ICME | 1979 | 2.54 | 0.90 | 21 | 599 | 1.7 |
| | | | | | | FF | ICME | 1979 | 9.13 | 0.93 | 77 | 191 | 1.4 |
| 1979 | 13.33 | 0.93 | 33 | 382 | 2.1 | FF | ICME | | | | | | |
| 1979 | 23.92 | 0.97 | 46 | 185 | 1.6 | FR | CIR | | | | | | |
| 1979 | 58.11 | 0.96 | 53 | 531 | 4.0 | FF | ICME | 1979 | 58.86 | 0.93 | 80 | 452 | 2.6 |
| 1979 | 62.08 | 0.94 | 70 | 965 | 6.9 | FF | ICME | 1979 | 62.40 | 0.92 | 81 | 368 | 1.7 |
| 1979 | 70.15 | 0.91 | 64 | 451 | 3.1 | FF | ICME | | | | | | |
| | | | | | | FF | ICME | 1979 | 79.19 | 0.81 | 84 | 506 | 2.6 |
| | | | | | | FF | ICME | 1979 | 80.72 | 0.80 | 14 | 538 | 1.1 |
| | | | | | | FF | ICME | 1979 | 86.37 | 0.75 | 89 | 784 | 4.6 |
| | | | | | | FF | ICME | 1979 | 92.84 | 0.68 | 42 | 480 | 2.8 |
| 1979 | 93.82 | 0.74 | 43 | 477 | 2.4 | FF | ICME | 1979 | 94.57 | 0.66 | 66 | 663 | 2.6 |
| 1979 | 112.56 | 0.53 | 82 | 524 | 1.5 | FF | CIR | | | | | | |
| 1979 | 347.37 | 0.54 | 31 | 397 | 2.0 | FF | ICME | 1979 | 347.52 | 0.69 | 27 | 467 | 2.1 |
| 1979 | 357.54 | 0.66 | 65 | 537 | 2.5 | FF | ICME | | | | | | |
| | | | | | | FF | ICME | 1979 | 364.66 | 0.84 | 67 | 434 | 2.1 |
| 1980 | 3.52 | 0.77 | 41 | 689 | 3.3 | FF | ICME | | | | | | |
| 1980 | 10.96 | 0.83 | 16 | 400 | 1.8 | FF | ICME | 1980 | 10.87 | 0.91 | 85 | 602 | 2.7 |
| 1980 | 26.93 | 0.92 | 63 | 94 | 3.4 | FR | CIR | 1980 | 24.88 | 0.96 | 35 | 387 | 1.2 |
| 1980 | 38.02 | 0.96 | 29 | 388 | 1.9 | FF | ICME | 1980 | 37.86 | 0.98 | 44 | 712 | 1.8 |

Table A1
(Continued)

| Helios 1 Observation | | | | | | Type | Driver | Helios 2 Observation | | | | | |
|----------------------|--------|-------|---------------|----------|----------|------|--------|----------------------|-------|-------|---------------|----------|----------|
| Year | DOY | r_h | θ_{Bn} | V_{sh} | M_{ms} | | | Year | DOY | r_h | θ_{Bn} | V_{sh} | M_{ms} |
| 1980 | 43.93 | 0.98 | 56 | 432 | 2.8 | FF | CIR | 1980 | 44.85 | 0.98 | 53 | 438 | 1.2 |
| 1980 | 60.62 | 0.98 | 79 | 532 | 2.0 | FF | ICME | | | | | | |
| 1980 | 65.07 | 0.98 | 40 | 525 | 2.5 | FF | ICME | 1980 | 65.61 | 0.93 | 79 | 485 | 1.7 |
| 1980 | 82.59 | 0.92 | 87 | 362 | 1.5 | FF | ICME | | | | | | |
| 1980 | 89.49 | 0.89 | 81 | 668 | 4.7 | FF | ICME | | | | | | |
| 1980 | 125.77 | 0.56 | 46 | 461 | 1.3 | FF | CIR | | | | | | |
| 1980 | 171.81 | 0.53 | 56 | 493 | 4.0 | FF | ICME | | | | | | |
| 1980 | 189.48 | 0.73 | 36 | 578 | 2.3 | FF | ICME | | | | | | |
| 1980 | 214.42 | 0.91 | 82 | 474 | 2.2 | FF | ICME | | | | | | |
| 1980 | 215.20 | 0.91 | 46 | 416 | 1.5 | FF | ICME | | | | | | |
| 1980 | 319.44 | 0.51 | 78 | 558 | 2.5 | FF | ICME | | | | | | |
| 1980 | 330.38 | 0.38 | 32 | 666 | 1.5 | FF | ICME | | | | | | |
| 1980 | 365.78 | 0.58 | 79 | 466 | 2.0 | FF | ICME | | | | | | |
| 1981 | 23.35 | 0.81 | 44 | 366 | 1.5 | FF | ICME | | | | | | |
| 1981 | 27.01 | 0.84 | 67 | 645 | 2.5 | FF | ICME | | | | | | |
| 1981 | 27.74 | 0.84 | 67 | 605 | 1.2 | FF | ICME | | | | | | |
| 1981 | 103.38 | 0.89 | 80 | 429 | 1.8 | FF | ICME | | | | | | |
| 1981 | 103.42 | 0.89 | 85 | 668 | 3.8 | FF | ICME | | | | | | |
| 1981 | 106.32 | 0.87 | 85 | 455 | 2.1 | FF | ICME | | | | | | |
| 1981 | 106.83 | 0.87 | 45 | 606 | 2.4 | FF | ICME | | | | | | |
| 1981 | 115.46 | 0.81 | 69 | 597 | 1.9 | FF | ICME | | | | | | |
| 1981 | 117.13 | 0.80 | 50 | 547 | 2.7 | FF | ICME | | | | | | |
| 1981 | 122.45 | 0.75 | 19 | 437 | 2.2 | FF | ICME | | | | | | |
| 1981 | 126.72 | 0.71 | 42 | 701 | 2.4 | FF | ICME | | | | | | |
| 1981 | 130.13 | 0.67 | 40 | 632 | 3.4 | FF | ICME | | | | | | |
| 1981 | 145.85 | 0.48 | 61 | 593 | 3.8 | FF | ICME | | | | | | |
| 1981 | 156.72 | 0.35 | 24 | 468 | 1.7 | FF | ICME | | | | | | |

Note. The shock encounter times by the spacecraft are given in the unit of day of year (DOY), where $DOY = \text{day} + (\text{hour}/24) + (\text{minute}/1440) + (\text{second}/86,400)$. r_h is given in the unit of au, θ_{Bn} in degree, and V_{sh} in km s^{-1} . The FR shocks are marked in bold font.

Acknowledgements

The work of R.H. is funded by the Chinese Academy of Sciences ‘‘Hundred Talents Program.’’ G.S.L. thanks the Indian National Science Academy, New Delhi, for the support under the INSA Honorary Scientist scheme. The work of Q.L. is supported by the National Science Foundation of China (NSFC) grants 42230201. The Helios measurements are collected from NASA’s Space Physics Data Facility (<https://spdf.gsfc.nasa.gov/>). The $F_{10.7}$ solar fluxes are obtained from the Laboratory for Atmospheric and Space Physics (LASP) Interactive Solar Irradiance Data Center (<https://lasp.colorado.edu/lisird/>).

Appendix

Table A1 lists all of the shocks under this study, their encounter times by the spacecraft, the types of the shocks, their interplanetary drives, and their characteristic parameters.

ORCID iDs

Rajkumar Hajra  <https://orcid.org/0000-0003-0447-1531>
Bruce T. Tsurutani  <https://orcid.org/0000-0002-0094-7224>
Quanming Lu  <https://orcid.org/0000-0003-3041-2682>
Lican Shan  <https://orcid.org/0000-0002-2354-9261>

References

Abraham-Shrauner, B. 1972, *JGR*, 77, 736

- Abraham-Shrauner, B., & Yun, S. H. 1976, *JGR*, 81, 2097
Anastasiadis, A., Lario, D., Papaioannou, A., Kouloumvakos, A., & Vourlidas, A. 2019, *RSPTA*, 377, 20180100
Balogh, A., Bothmer, V., Crooker, N., et al. 1999, *SSRv*, 89, 141
Barnes, C. W., & Simpson, J. A. 1976, *ApJL*, 210, L91
Belcher, J. W., & Davis, L. 1971, *JGR*, 76, 3534
Bougeret, J. L., King, J. H., & Schwenn, R. 1984, *SoPh*, 90, 401
Burlaga, L., Fitzenreiter, R., Lepping, R., et al. 1998, *JGR*, 103, 277
Burlaga, L., Sittler, E., Mariani, F., & Schwenn, R. 1981, *JGRA*, 86, 6673
Chen, J., & Krall, J. 2003, *JGRA*, 108, 1410
Dasgupta, B., Tsurutani, B. T., & Janaki, M. S. 2003, *GeoRL*, 30, 2128
Desai, M., & Giacalone, J. 2016, *LRSP*, 13, 3
Dryer, M. 1975, *SSRv*, 17, 277
Echer, E. 2019, *GeoRL*, 46, 5681
Gloeckler, G., Geiss, J., & Fisk, L. A. 2001, in *The Heliosphere Near Solar Minimum. The Ulysses Perspective*, ed. A. Balogh, R. G. Marsden, & E. J. Smith (London: Springer-Praxis), 287
Gloeckler, G., Jokipii, J. R., Giacalone, J., & Geiss, J. 1994, *GeoRL*, 21, 1565
Gold, T. 1955, in *Gas Dynamics of Cosmic Clouds*, ed. H. C. van de Hulst & J. M. Burgers (Amsterdam: NHP), 103
González-Esparza, J. A., Neugebauer, M., Smith, E. J., & Phillips, J. L. 1998, *JGR*, 103, 4767
Hajra, R. 2021, *ApJ*, 917, 91
Hajra, R., & Sunny, J. V. 2022, *SoPh*, 297, 30
Hellinger, P., Matteini, L., Štverák, Š., Trávníček, P. M., & Marsch, E. 2011, *JGRA*, 116, A09105
Hellinger, P., Trávníček, P. M., Štverák, Š., Matteini, L., & Velli, M. 2013, *JGRA*, 118, 1351
Hoang, S., Lacombe, C., Mangeney, A., et al. 1995, *AdSpR*, 15, 371
Hudson, P. D. 1970, *P&SS*, 18, 1611
Hugoniot, H. 1887, *J. Ec. Polytech.*, 57, 3
Hugoniot, H. 1889, *J. Ec. Polytech.*, 58, 1
Jian, L., Russell, C. T., Luhmann, J. G., & Skoug, R. M. 2006, *SoPh*, 239, 337
Kallenrode, M. B. 2003, *JPhG*, 29, 965

- Kennel, C. F., Edmiston, J. P., & Hada, T. 1985, in *Collisionless Shocks in the Heliosphere: A Tutorial Review*, ed. R. G. Stone & B. T. Tsurutani (Washington, DC: American Geophysical Union), 1
- Khazanov, G. V., Moore, T. E., Krivorutsky, E. N., Horwitz, J. L., & Liemohn, M. W. 1996, *GeoRL*, **23**, 797
- Khazanov, I., & Singh, N. 2007, *GeoRL*, **34**, L20111
- Lepping, R. P., & Behannon, K. W. 1986, *JGR*, **91**, 8725
- Lundin, R., & Guglielmi, A. 2006, *SSRv*, **127**, 1
- Mariani, F., Ness, N. F., Burlaga, L. F., Bavassano, B., & Villante, U. 1978, *JGR*, **83**, 5161
- Marsch, E. 2012, *SSRv*, **172**, 23
- Marsch, E., Mühlhäuser, K.-H., & Schwenn, R. 1982a, *JGR*, **87**, 52
- Marsch, E., Mühlhäuser, K.-H., Rosenbauer, H., Schwenn, R., & Neubauer, F. M. 1982b, *JGR*, **87**, 35
- McDonald, F. B., Teegarden, B. J., Trainor, J. H., Von Roseninge, T. T., & Webber, W. R. 1975, *ApJL*, **203**, L149
- Neugebauer, M. 2013, *SSRv*, **176**, 125
- Papadopoulos, K. 1985, in *Collisionless Shocks in the Heliosphere: A Tutorial Review*, ed. R. G. Stone & B. T. Tsurutani (Washington, DC: American Geophysical Union), 59
- Parker, E. N. 1958, *ApJ*, **128**, 664
- Pesses, M. E., Tsurutani, B. T., Van Allen, J. A., & Smith, E. J. 1979, *JGR*, **84**, 7297
- Pesses, M. E., Van Allen, J. A., & Goertz, C. K. 1978, *JGR*, **83**, 553
- Pitňa, A., Šafránková, J., Němeček, Z., Ďurovcová, T., & Kis, A. 2021, *FrP*, **8**, 626768
- Pizzo, V. J. 1985, in *Collisionless Shocks in the Heliosphere: Reviews of Current Research*, Geophysical Monograph Series, ed. B. T. Tsurutani & R. G. Stone, Vol. 35 (Washington, DC: American Geophysical Union), 51
- Rankine, W. J. M. 1870, *RSPT*, **160**, 277
- Reames, D. V. 1999, *SSRv*, **90**, 413
- Reames, D. V. 2013, *SSRv*, **175**, 53
- Richardson, J. D., & Wang, C. 2005, in *AIP Conf. Proc. 781, The Physics of Collisionless Shocks: 4th Annual IGPP Int. Astrophysics Conf.* (New York: AIP), 278
- Sagdeev, R. Z. 1966, in *Reviews of Plasma Physics*, ed. M. A. Leontovich (New York: Consultants Bureau), 23
- Sakai, J. I., Yamamura, W., & Saito, S. 2005, *NJPh*, **7**, 233
- Smith, E. J., & Wolfe, J. H. 1976, *GeoRL*, **3**, 137
- Smolyakov, A. I., Sydorenko, D., & Froese, A. 2007, *PPCF*, **49**, A221
- Temmer, M., Veronig, A. M., Kontar, E. P., Krucker, S., & Vršnak, B. 2010, *ApJ*, **712**, 1410
- Thomas, B. T., & Smith, E. J. 1981, *JGR*, **86**, 11105
- Tsurutani, B. T., Arballo, J. K., Lakhina, G. S., et al. 1998, *GeoRL*, **25**, 3047
- Tsurutani, B. T., Dasgupta, B., Galvan, C., et al. 2002, *GeoRL*, **29**, 2233
- Tsurutani, B. T., Gonzalez, W. D., Gonzalez, A. L. C., et al. 1995a, *JGR*, **100**, 21717
- Tsurutani, B. T., Gonzalez, W. D., Tang, F., et al. 1990, *P&SS*, **38**, 109
- Tsurutani, B. T., Gonzalez, W. D., Tang, F., Akasofu, S. I., & Smith, E. J. 1988, *JGR*, **93**, 8519
- Tsurutani, B. T., & Ho, C. M. 1999, *RvGeo*, **37**, 517
- Tsurutani, B. T., Ho, C. M., Arballo, J. K., Goldstein, B. E., & Balogh, A. 1995b, *GeoRL*, **22**, 3397
- Tsurutani, B. T., Lakhina, G. S., Verkhoglyadova, O. P., et al. 2011, *JASTP*, **73**, 5
- Tsurutani, B. T., & Lin, R. P. 1985, *JGR*, **90**, 1
- Tsurutani, B. T., Richardson, I. G., & Thorne, R. M. 1985, *JGR*, **90**, 12159
- Tsurutani, B. T., Shan, L., Lakhina, G. S., et al. 2021, *A&A*, **656**, A152
- Tsurutani, B. T., & Smith, E. J. 1979, *JGR*, **84**, 2773
- Tsurutani, B. T., Smith, E. J., Pyle, K. R., & Simpson, J. A. 1982, *JGR*, **87**, 7389
- Tsurutani, B. T., Wu, S. T., Zhang, T. X., & Dryer, M. 2003, *A&A*, **412**, 293
- Tsurutani, B. T., Zank, G. P., Sterken, V. J., et al. 2023, *ITPS*
- Van Hollebeke, M. A. I., MaSung, L. S., & McDonald, F. B. 1975, *SoPh*, **4**, 189
- Venzmer, M. S., & Bothmer, V. 2018, *A&A*, **611**, A36
- Verkhoglyadova, O. P., Li, G., Zank, G. P., et al. 2010, *JGRA*, **115**, A12103
- Zank, G. P., Li, G., & Florinski, V. 2006, *JGRA*, **111**, A06108
- Zhang, J., Dere, K. P., Howard, R. A., & Vourlidas, A. 2004, *ApJ*, **604**, 420
- Zhuang, B., Lugaz, N., Temmer, M., Gou, T., & Al-Haddad, N. 2022, *ApJ*, **933**, 169